Journal of Materials Science & Technology 35 (2019) 231–238

Contents lists available at ScienceDirect

Journal of Materials Science & Technology

journal homepage: www.jmst.org

Research Article

Understanding of degradation-resistant behavior of nanostructured thermal barrier coatings with bimodal structure

Guangrong Li[a,b], Guanjun Yang[a,*]

[a] State Key Laboratory for Mechanical Behavior of Materials, School of Materials Science and Engineering, Xi'an Jiaotong University, Xi'an, 710049, China
[b] State Key Laboratory for Manufacturing Systems Engineering, School of Mechanical Engineering, Xi'an Jiaotong University, Xi'an, 710049, China

ARTICLE INFO

Article history:
Received 23 May 2018
Received in revised form 12 June 2018
Accepted 19 June 2018
Available online 25 September 2018

Keywords:
Thermal barrier coatings (TBCs)
Bimodal structure
Degradation-resistance
Structural tailoring

ABSTRACT

Nanostructured thermal barrier coatings (TBCs) often provide high degradation resistance, as well as extended lifetime. However, the underlying mechanism has not been fully understood. In this study, the sintering characteristics of nanostructured yttria-stabilized zirconia (YSZ) coatings were investigated, and compared with those of the conventional YSZ coatings. Multiscale characterizations of the changes in microstructures and properties were performed. Results showed that the enhanced high-performance durability was mainly attributed to different sintering mechanisms of lamellar zones and nanozones. Sintering characteristics of the lamellar zones were similar to those of the conventional coatings. Stage-sensitive healing of two-dimensional (2D) pores dominated the sintering behavior of the lamellar zones. However, the differential densification rates between nanozones and lamellar zones of the nanostructured TBCs led to the formation of coarse voids. This counteractive effect, against healing of 2D pores, was the main factor contributing to the retardation of the performance degradation of bimodal TBCs during thermal exposure. Based on the understanding of the performance-degradation resistance, an outlook towards TBCs with higher performances was presented.

1. Introduction

Thermal barrier coatings (TBCs) are protective layers applied to the surfaces of hot metallic components in gas turbine engines, which are frequently utilized in aircraft propulsion and power generation [1–8]. TBCs can cool down the underlying substrate, leading to improved component durability. Meanwhile, fuel efficiency can be increased by allowing an increase in the inlet temperature in a turbine. Commonly, a TBC consists of a ceramic top coat, a metallic bond coat, and a thermally grown oxide (TGO) layer forming at operation temperatures. Regarding the function and durability of TBCs, the performances of thermal insulation and resistance to spallation during high-temperature services are crucial [9–13]. The top coat acts as a thermal barrier, and thereby has a major influence on the performances of TBCs.

Top coats are usually prepared by plasma spraying (PS) and electron beam-physical vapor deposition (EB-PVD). The high investment cost and low deposition efficiency make EB-PVD a very expensive process [14]. In contrast, PS is cost-effective, and thereby more commonly applied in the fabrication of TBCs. PS ceramic coatings exhibit a typical lamellar structure with different types of pores (or cracks) [15–18]. The inter-splat pores correspond to the imperfect bonding between layers. Their orientations are against the heat flux, and dominantly responsible for the thermal insulation. Intra-splat cracks refer to the cracks inside an originally disk-shaped splat. They run through the splat thickness. The inter-splat pores are connected with intra-splat cracks, leading to a two-dimensional (2D) pore network. Therefore, values of thermal and mechanical properties of PS top coat are only <50% of those of the corresponding bulk materials [19–21]. For example, the through-thickness thermal conductivity of PS yttria-stabilized zirconia (YSZ) is approximately 1 W m^{-1} K^{-1}, whereas that of bulk YSZ is 2.5 W m^{-1} K^{-1} [22]. Similarly, the macroscopic in-plane elastic modulus of YSZ is approximately 20 GPa, while the corresponding value of bulk YSZ is ~220 GPa [23]. The very low values of thermal conductivity and elastic modulus, compared with bulk YSZ material, suggest that PS top coat has excellent thermal insulation and strain tolerance at its as-deposited state. However, the lifetime of PS top coat is significantly shorter than that of EB-PVD top coat [24,25]. One of the reasons is that sintering leads to stiffening of the top coat during thermal exposure [26]. It was reported that the in-plane elastic modulus can be increased by 200% after heat treat-

* Corresponding author.
E-mail address: ygj@mail.xjtu.edu.cn (G. Yang).

https://doi.org/10.1016/j.jmst.2018.09.054
1005-0302/

ment at 1300 °C for 100 h [23,27]. As a result, the strain tolerance would be significantly affected and some large cracks are formed subsequently, resulting in the spallation of the top coat [28,29]. Therefore, the performance degradation induced by sintering is a main concern during the service of a PS top coat [30].

A PS nanostructured top coat seems to be a good choice to retard the performance degradation [31–35]. It has been reported that the degradation degree of the thermal insulation of a nanostructured YSZ coating is <50% of that of the conventional PS YSZ coating [36,37]. In addition, the lifetime of nanostructured coatings is extended by 50%–100% [38,39]; the oxidation resistance is enhanced significantly as well [40]. However, the underlying mechanism responsible for the degradation-resistant behavior of the PS nanostructured top coat has not been fully understood. In previous studies, failure of TBCs was highly related to the structural evolution during thermal exposure [28] and the thermal stress caused by thermal mismatch between metallic layer and ceramic layer [41]. PS nanostructured top coat often exhibits a bimodal structure: un-melted nanozones are surrounded by melted lamellar zones [40,42,43]. This unique microstructure complicates the structural evolution of nanostructured top coat, compared to that of the conventional lamellar top coat. The nanozones have a higher surface area with an isotropic loose structure, whereas the lamellar zones are relatively denser with an anisotropic structure [44]. Therefore, sintering behavior of lamellar zones would be different from that of nanozones. The final performance would be a comprehensive reflection of the structural evolution of the bimodal structure. Therefore, it is necessary to reveal the sintering characteristics of bimodal structures to understand the degradation-resistant behavior of nanostructured TBCs.

This study compared the structural evolutions of conventional lamellar and nanostructured bimodal coatings. Sintering characteristics of both lamellar zones and nanozones were characterized by a systematical investigation of the changes of microstructures and properties during thermal exposure. The mechanism responsible for the degradation-resistant behavior was revealed. In addition, an outlook on structural tailoring towards high performance TBCs was proposed.

2. Experimental

2.1. Sample preparation

Conventional lamellar top coat was prepared by a commercially available hollow spheroidized YSZ powder (HOSP, -75-45 μm, Metco 204B-NS, Sulzer Metco Inc., New York, USA). Nanostructured bimodal top coat was prepared by a commercial nanostructured YSZ (Nanox S4007, Inframat corporation, Farmington, CT, USA). A spray drying process was used to agglomerate individual nanosized YSZ powders into microscopic agglomerates, which can be sprayed effectively. A laser diffraction particle size analyzer (Beckman Coulter, Miami, FL, USA) was used to evaluate size distribution of the agglomerates, while a Nano measurer was used to determine size distribution of the nanopowders. Morphologies and particle size distribution of the agglomerates and nanosized powders are shown in Fig. 1 [45]. Such two types of YSZ coatings were deposited on stainless-steel substrates to ~1 mm, using a commercial plasma spray system (GP-80, 80 kW class, Jiujiang, China). The spray parameters are shown in Table 1. After deposition, free-standing samples were obtained through dissolution of substrate by a hydrochloric acid solution. In order to remove residual acid in coatings, free-standing samples were further immersed in deionized water for 24 h.

Table 1
Parameters used for plasma spraying.

Parameter	Value
Plasma arc voltage (V)	60
Plasma arc current (A)	650
Flow rate of primary gas (Ar) ($L\,min^{-1}$)	50
Flow rate of secondary gas (H_2) ($L\,min^{-1}$)	7
Flow rate of powder feeding gas (N_2) ($L\,min^{-1}$)	4.5
Spray distance (mm)	100
Torch traverse speed ($mm\,s^{-1}$)	500

2.2. Structural characterization

Service temperatures of TBCs with YSZ top coat are often under 1200 °C to avoid significant formation of monoclinic phase [46,47]. Therefore, thermal exposure was conducted in an isothermal furnace at 1150 °C with heating and cooling rates of 10 °C min^{-1}.

Scanning electron microscopy (SEM, TESCAN MIRA 3, Czech) was used to characterize surface and cross-sectional morphology of the samples. Healing of 2D pores was examined by two methods, since 2D pores dominantly determine the thermal and mechanical properties of PS top coat. One is quasi in-situ observation by SEM, and the other one is quantitative characterization by statistical 2D pore density. Detail for these two methods can be found elsewhere [48,49], and would be briefly described herein. The key for quasi in-situ observation is to repeatedly find the target position at high magnifications after different thermal exposure durations. Therefore, the general procedure is as follows: (i) a target position is found at a high magnification; (ii) the corresponding position is labeled at a low magnification; (iii) the target position can be re-located according to its labels after thermal exposure. 2D pore density refers to the statistical 2D pore length in a unit area. At least 20 SEM images with a magnification of 5000 times were used. In addition to 2D pore density, apparent porosity was determined by image analysis using SEM backscattered electron images with a magnification of 1000 times. For each state during thermal exposure, 10 images were used to estimate the apparent porosity.

2.3. Properties determination

The complicated structure of PS ceramic coating makes it difficult to determine the properties effectively in a single way, since the properties are actually scale-sensitive. Therefore, both macroscopic and microscopic elastic moduli in their in-plane directions were determined. The reason is that thermal stress caused by substrate is mainly generated in the in-plane direction [28,48,50,51]. Macroscopic elastic modulus was determined by three-point bending (Instron 5943, America) at samples with dimensions of 60 mm × 10 mm × 1 mm. A dialgauge on the measurement device was used to determine central deflection (w). Subsequently, macroscopic elastic modulus (E) can be obtained from the following formulas:

$$w = \frac{PL^3}{48D} \tag{1}$$

$$D = \frac{E_y h^3}{12(1-\nu^2)} \tag{2}$$

where P is the load applied at the middle of the span, L is the span between two supports, D is the bending stiffness, E_y is the Young's moduli of the coating, h is the coating thickness, ν is the Poisson's ratio of the coating, and w is the central deflection.

Microscopic elastic modulus was determined by Knoop indentation (Buehler, Micromet 5104, Akashi Corporation, Japan). The sample size is Φ20 mm × 1 mm. The load was 0.3 kg and duration

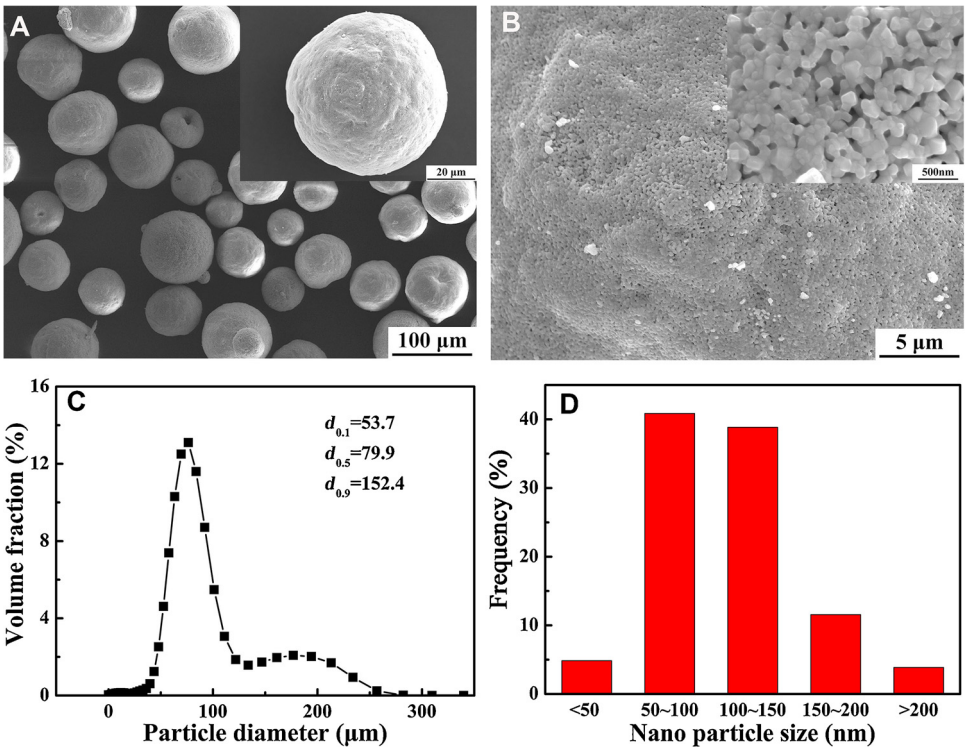

Fig. 1. Morphologies and size distributions of agglomerates and nanosized powders [45]: (A) morphology of agglomerates; (B) surface morphology of agglomerates with nanosized powders; (C) size distribution of agglomerates; (D) size distribution of nanosized primary particles ($d_{0.1}$: 10% particles have diameters smaller than the value 53.7 μm; $d_{0.5}$: 50% particles have diameters smaller than the value 79.9 μm; $d_{0.9}$: 90% particles have diameters smaller than the value 152.4 μm).

was 30 s. In-plane elastic modulus was determined from the polished surface. The formula to determine the elastic modulus is:

$$E = \frac{\alpha H}{(\frac{b}{a} - \frac{b'}{a'})} \tag{3}$$

where α is a constant (0.45), H is hardness, a' and b' are the lengths of the major and minor diagonals of the indentation impression, respectively, a and b are the lengths of the major and minor diagonals of the indenter, respectively, and b/a is 1/7.11.

Thermal conductivity was determined by a laser flash method. The sample size was Φ12.7 mm × 1 mm. The thermal diffusivity of samples was measured using a laser flash analyzer (Netzsch, Germany) at high temperature of 900 °C. Three samples were used to determine the thermal diffusivity of each state during thermal exposure. Heat capacity of the coatings was determined using differential scanning calorimetry 404 (Netzsch, Germany) and density was calculated by dividing mass of the sample by its volume. Subsequently, thermal conductivity can be calculated using the following equation:

$$\lambda = \rho \cdot C_P \cdot \alpha_t \tag{4}$$

where λ is the calculated thermal conductivity, ρ is the density, C_P is the heat capacity, and α_t is the thermal diffusivity.

3. Results

3.1. Global structural evolution

Fig. 2 shows the polished cross-sections of the samples after progressively increasing the thermal-exposure duration. At the as-deposited state, the conventional sample exhibits a typical lamellar structure with inter-splat pores and intra-splat cracks. In contrast, the nanostructured sample exhibits a bimodal structure, which implies that medium gray nanozones are surrounded by the lighter lamellar zones. Moreover, the lamellar zone in the nanostructured samples is similar to that in the conventional samples. Regarding the structural evolution of the conventional samples, the number of large-sized pores (approximate size of 5–15 μm) observed at the as-deposited state decreases distinctly during the thermal exposure. Regarding the structural evolution of the nanostructured samples, the contrast between the nanozone and lamellar zone is not as distinct as in the as-deposited state. This may be attributed to the sintering occurring in both lamellar zones and nanozones.

3.2. Overall evolution of mechanical property

Fig. 3 shows the changes of the in-plane elastic modulus as a function of the thermal-exposure duration. Common phenomena can be observed for the conventional and nanostructured samples. The elastic modulus exhibits a significant increase, at macroscale and microscale. Moreover, the evolution exhibits an obvious non-linear trend. A very rapid increase occurs at initial short exposure durations, while a gradual increase could be observed at following long exposure durations. Therefore, the increment mainly occurs during the initial exposure. The comparison between the conventional and nanostructured samples reveals that the elastic moduli at the as-deposited states are comparable. However, the increments in the nanostructured samples are lower than those of the conventional samples. This suggests that the nanostructured samples, to some degree, can retard the sintering-induced stiffening.

3.3. Overall evolution of thermal conductivity

Fig. 4 shows the changes in the thermal conductivity as a function of the thermal-exposure duration. A similarity between the mechanical and thermal properties could be observed; the evolution trends of the thermal conductivity are also non-linear. Therefore, the fast increase at initial short durations turns into a

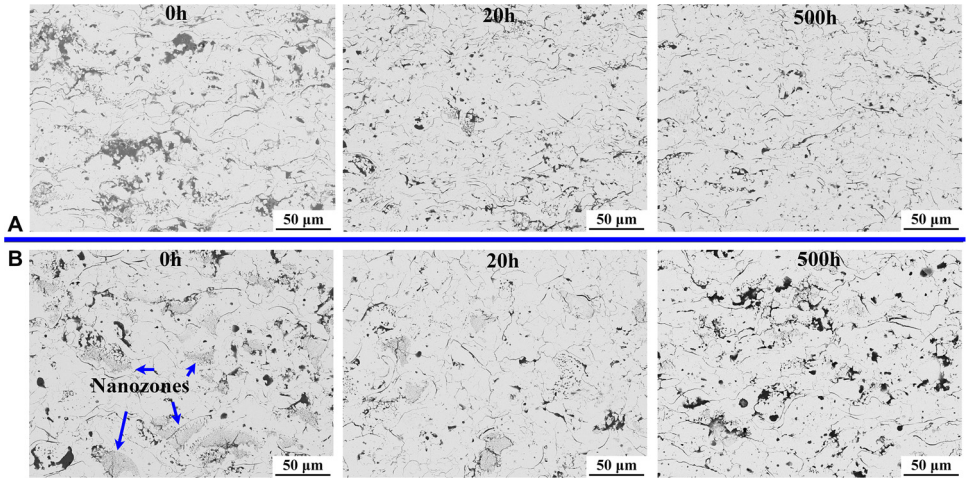

Fig. 2. Global structural evolution during thermal exposure: (A) conventional TBCs; (B) nanostructured TBCs.

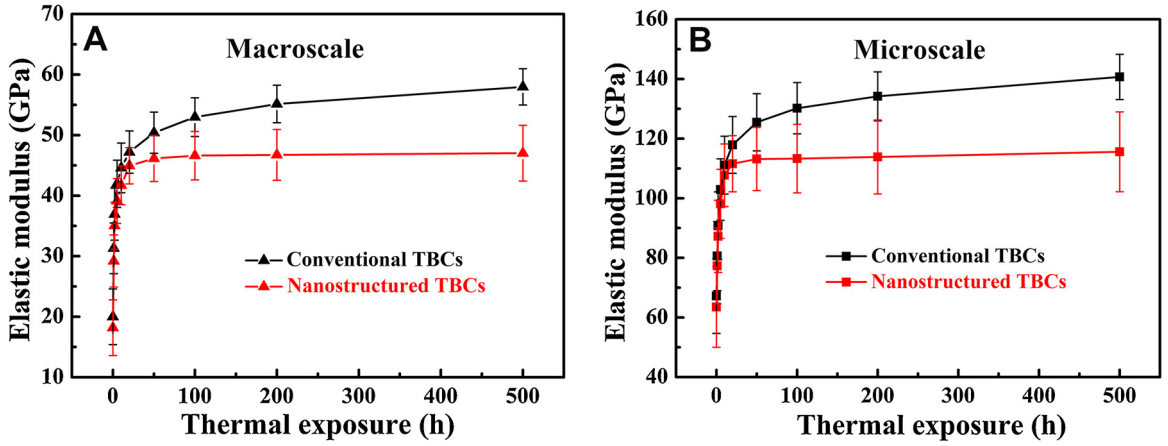

Fig. 3. Changes of elastic modulus as a function of thermal exposure duration: (A) macroscale; (B) microscale.

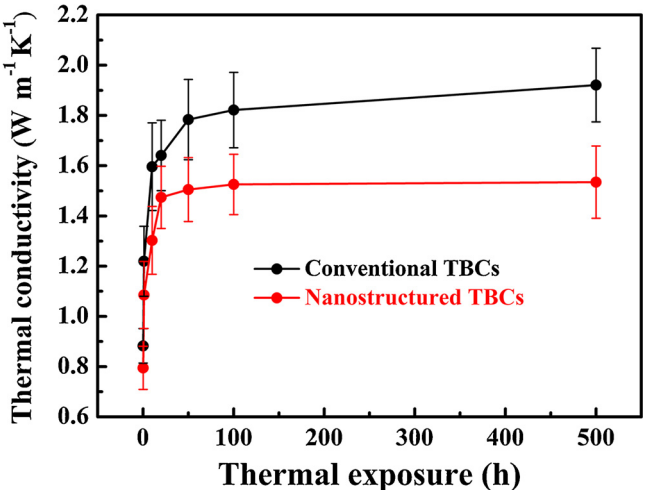

Fig. 4. Changes of thermal conductivity as a function of thermal-exposure duration.

significantly slower increase at long exposure durations. The comparison between the conventional and the nanostructured samples reveals that the nanostructured samples exhibit a slightly lower thermal conductivity at the as-deposited state. Moreover, it is clear that the increase in the nanostructured samples is not as significant as that of the conventional ones after long durations. Therefore, the nanostructured coatings weaken the degradation of the thermal insulation during thermal exposure.

4. Discussion

4.1. Sintering characteristics of lamellar zones

Evolutions of the thermal and mechanical properties of nanostructured TBCs are a comprehensive reflection of lamellar zones and nanozones. Therefore, it is necessary to understand the sintering characteristics of these two zones. For the lamellar zones, the inter-splat pores and intra-splat cracks dominantly determine the effective properties [16,22,48]. Fig. 5 shows the statistical 2D pore density as a function of the thermal-exposure duration. In order to clearly show the changes at the initial short exposure durations, double-logarithmic plots were used. In addition, the value of 0.1 h was used to represent the as-sprayed state (corresponding to 0 h), in order to show the overall evolution [26]. Healing characteristics of the lamellar zones of the nanostructured samples are similar to those of conventional samples. Densities of the inter-splat pores and intra-splat cracks significantly decreased during the overall thermal exposure, which results in the obvious changes in the thermal and mechanical properties. The double-logarithmic plots reveal that the changes of the 2D pore density were stage-sensitive. At stage I (~20 h), the healing kinetics of the inter-splat pores was significantly faster, whereas the intra-splat cracks seemed unaffected. At stage II, both inter-splat pores

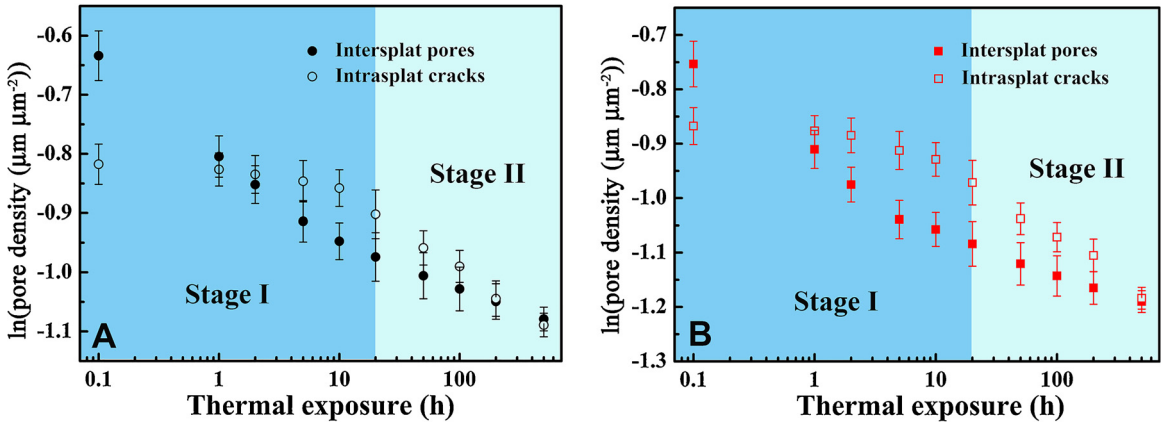

Fig. 5. Statistical 2D pore densities during thermal exposure: (A) conventional TBCs; (B) nanostructured TBCs.

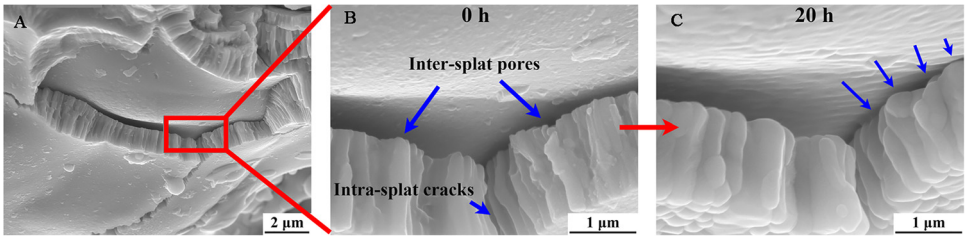

Fig. 6. Quasi in-situ healing behavior of an inter-splat pore at lamellar zones: (A) inter-splat pore at 0 h; (B) local region of inter-splat pore at 0 h; (C) local region of inter-splat pore after thermal exposure for 20 h.

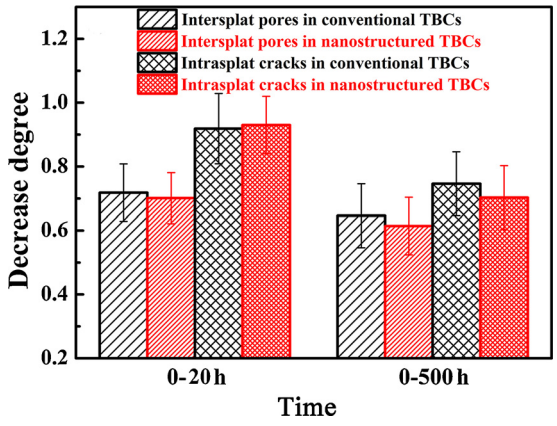

Fig. 7. Comparison of decrease degrees of 2D pore density at different stages.

and intra-splat cracks were healed at a similar but significantly slower rate. The significantly faster healing of the inter-splat pores at stage I was mainly attributed to the materials and structures. Fig. 6 shows the quasi-in-situ healing of the inter-splat pores. It was found that the inter-splat pores exhibited wedge-like morphology. The initially flat splat surface gradually became roughening, leading to multipoint contacts at the very narrow pore tips. This would provide multi-way diffusion for matter transfer. Consequently, a significantly faster sintering kinetic occurs at stage I, as the sintering process of ceramics was driven by the decrease in the free energy of the whole system. At stage II, it is challenging to realize further multi-contact, as the unhealed parts are relatively wider. Therefore, the matter transfer can only proceed in a single way, leading to a significantly slower sintering kinetics.

Fig. 7 shows comparisons of the decreasing degrees of 2D pores with respect to their corresponding as-deposited values. It can be found that the drop degrees of 2D pores in the nanostructured samples were very similar to those in the conventional ones. Therefore, it can be concluded that the sintering behavior of the lamellar zones in the nanostructured samples was similar to that in the conventional samples. The healing of 2D pores was the main factor contributing to the stiffening of the coatings [52,53]. Moreover, the significant healing of the inter-splat pores is responsible for the ultra-fast sintering kinetics observed by the changes of the thermal and mechanical properties (see Figs. 3 and 4). Subsequently, at stage II, the healing of the inter-splat pores and intra-splat cracks proceeded at a lower rate.

4.2. Sintering characteristics of interface between lamellar zones and nanozones

The above results and discussion reveal that the changes in the lamellar zones are not an essential cause for the differential evolution trends between the nanostructured and conventional samples. Therefore, this section focuses on the sintering-induced changes in the nanozones.

The nanozones have distinct effects on the properties at the as-deposited state and states after the thermal exposure. For the as-deposited state, the nanozones refer to the porous nanostructured agglomerates. The large quantity of micropores in the nanozones enhanced the thermal insulation performance, which explains the lower thermal conductivity of nanostructured coatings than that of conventional coatings [36]. For the states after the thermal exposure, the presence of micropores significantly increased the surface energy. Consequently, the porous nanozones have a higher driving force than that of the lamellar zones with respect to sintering-induced densification. Fig. 8 shows the interfacial evolution between the lamellar zones and nanozones during the thermal exposure. The sintering led to link-up of nanozones and lamellar zones at some parts. This could be responsible for the phenomenon of gradual decrease observed in Fig. 2. Moreover, the faster densification of the nanozones led to the separation of nanozones and

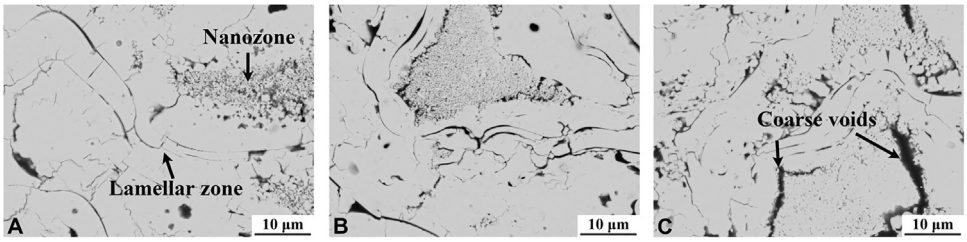

Fig. 8. Interfacial evolution between nanozones and lamellar zones during thermal exposure: (A) as-deposited state; (B) 20 h; (C) 500 h.

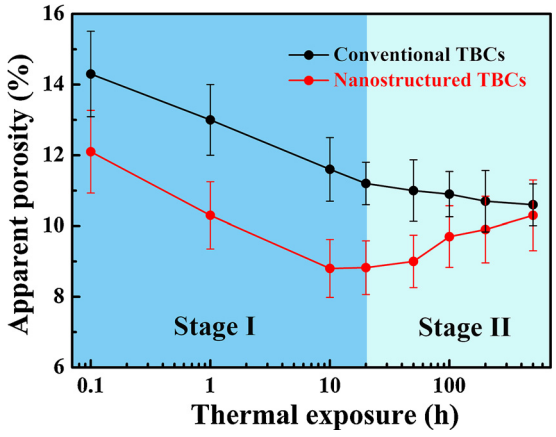

Fig. 9. Comparison of apparent porosities between conventional TBCs and nanostructured TBCs during thermal exposure.

lamellar zones, and consequently to formation of coarse voids. The activation energy of the grain growth in nanozones can be obtained as follows [54]:

$$D_t = D_0 \exp(\frac{-Q}{RT}) \quad (5)$$

where D_0 and D_t are the initial and final nanocrystallite sizes, R is the molar gas constant, and T is the annealing temperature.

The obtained activation energy of the grain growth was approximately 10 kJ/mol; the corresponding energy for bulk YSZ is approximately 580 kJ mol^{-1} [54]. Therefore, the very low activation energy of the grain growth is a characteristic of nanocrystalline ceramic oxides. This can be responsible for the different densification rates between lamellar zones and nanozones. These coarse voids can counteract the negative effect of the healing of microscopic pores (including 2D pores in lamellar zones and micropores in nanozones).

Fig. 9 shows comparisons of the changes in apparent porosity after thermal exposure. At stage I, apparent porosities decreased with a similar trend for the nanostructured and conventional samples, which could be attributed to the significant healing of inter-splat pores (see Fig. 5). At the as-deposited state, the main contribution to porosity is the large pores observed in Fig. 2. These large pores emerged from spalling-off weakly bonded splats during the sample preparation [55]. After the thermal exposure, the healing of the inter-splat pores enhanced the bonding between splats, and consequently the quantity of large pores is decreased. At stage II, the porosity of the nanostructured samples increased, whereas the porosity of the conventional sample slightly decreased. This is attributed to the formation of coarse voids caused by the differential densification rates between the lamellar zones and nanozones.

4.3. Mechanism of degradation resistance of nanostructured TBCs

Based on the sintering characteristics of lamellar zones and nanozones, it is possible to understand the performance-degradation-resistant behavior of nanostructured bimodal TBCs. Fig. 10 shows the changes of the mechanical properties in double-logarithmic plots. The evolution trends of the properties also exhibit two-stage characteristics. The increase rates at stage I are significantly higher than those at stage II. Correspondingly, Fig. 11 shows the normalized increments in the properties' values with respect to those of the as-deposited states. The increments in elastic modulus at stage I of the nanostructured and conventional samples are comparable, since the healing of inter-splat pores is the dominant structural change at this stage (Fig. 5). However, at long exposures (stage II), coarse voids appear inside the nanostructured coatings. Therefore, the increments in elastic modulus are not as significant as those of conventional coatings.

From the comprehensive comparison of the sintering behavior of the lamellar zones and nanozones, it can be concluded that the degradation-resistant behavior of nanostructured bimodal TBCs is mainly attributed to the formation of coarse voids, which positively affect the effective thermal and mechanical properties. Using energy of the whole system, the following equation determines whether cracks would propagate [28]:

$$G_i > G_{ic} \quad (6)$$

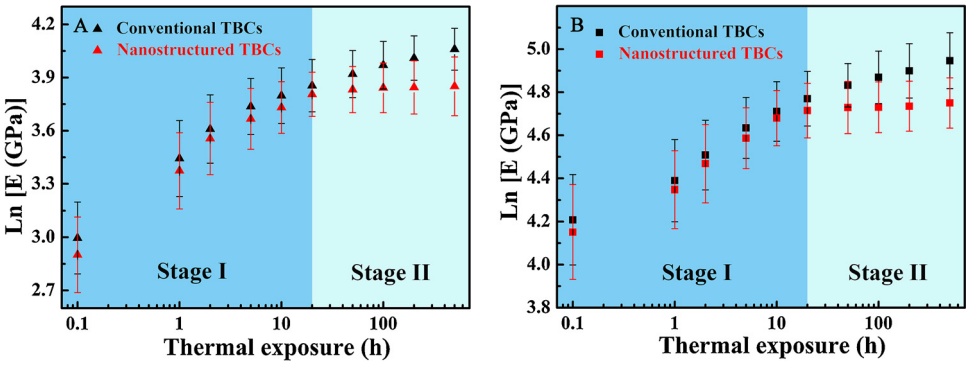

Fig. 10. Changes of elastic modulus in double logarithmic plots: (A) macroscale; (B) microscale.

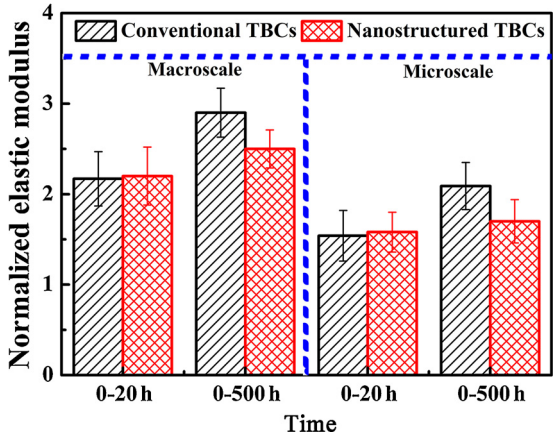

Fig. 11. Comparison of normalized elastic modulus with respect to their as-deposited states.

$$G_i = \int_0^h \frac{E\varepsilon^2}{2(1-\upsilon)} dh \quad (7)$$

where G_i is the strain-energy release rate, G_{ic} is the critical strain-energy release rate, h is the vertical distance from the coating surface to the position of the crack, and ε is the strain.

The nanostructured TBCs retard the stiffening process. The lower elastic modulus leads to a weaker driving force for the spallation of the top coat, which can explain their extended lifetime.

In summary, the degradation-resistant behavior of nanostructured bimodal TBCs was significantly related to the sintering of lamellar zones and nanozones. The healing of 2D pores in lamellar zones led to a significant improvement of the effective thermal and mechanical properties; the coarse voids emerging from the differential densification rates between nanozones and lamellar zones counteracted the performance degradation. It is worth noting that the nanozones in PS nanostructured coatings are in isotropic forms. Therefore, the orientation of the coarse voids would be randomly distributed. The orientation of pores in TBCs would have a significant effect on the thermal and mechanical properties [13,15]. Therefore, in future studies, it is necessary to control the orientation of the newly formed pores; a hybrid spray method may be a promising approach. In this method, the lamellar zones are deposited by conventional air plasma spraying, whereas the nanozones would be deposited by suspension plasma spraying. The obtained nanozones would be in anisotropic forms, as the stacked splats. Therefore, the orientation of the newly formed pores can be controlled, and the performance of thermal insulation and lifetime can be further optimized.

5. Conclusions

A detailed study on the sintering characteristics of PS nanostructured bimodal TBCs was performed to understand their performance-degradation-resistant behavior. The enhanced high-performance durability was mainly attributed to the different sintering mechanisms of the lamellar zones and nanozones. The following conclusions of this study can be summarized:

(1) Stage-sensitive healing of 2D pores was the main sintering characteristic of lamellar zones. The fast healing of inter-splat pores led to the ultrafast sintering kinetic at stage I, responsible for the significant improvements in the thermal and mechanical properties. This is similar to the behavior in conventional TBCs.
(2) The differential densification rates between nanozones and lamellar zones led to the formation of coarse voids, which counteracted the effect of the healing of 2D pores in lamellar zones. This was the main factor, which retarded the performance degradation of bimodal TBCs during thermal exposure.

Acknowledgements

This work was supported financially by the National Natural Science Foundation of China (Nos. 51801148, 51671159), the China Postdoctoral Science Foundation (No. 2018M631151), the National Basic Research Program of China (No. 2013CB035701), the Fundamental Research Funds for the Central Universities, and the National Program for Support of Top-notch Young Professionals.

References

[1] N.P. Padture, Nat. Mater. 15 (2016) 804–809.
[2] W.Z. Tang, L. Yang, W. Zhu, Y.C. Zhou, J.W. Guo, C. Lu, J. Mater. Sci. Technol. 32 (2016) 452–458.
[3] L. Guo, M.Z. Li, Y. Zhang, F.X. Ye, J. Mater. Sci. Technol. 32 (2016) 28–33.
[4] X.X. Zhao, L. Guo, C.M. Wang, Y. Zhang, F.X. Ye, J. Mater. Sci. Technol. 33 (2017) 192–197.
[5] W.W. Zhang, G.R. Li, Q. Zhang, G.J. Yang, J. Adv. Ceram. 6 (2017) 230–239.
[6] L. Chen, G.J. Yang, J. Adv. Ceram. 7 (2018) 17–29.
[7] X.G. Chen, H.M. Zhang, H.S. Zhang, Y.D. Zhao, G. Li, J. Adv. Ceram. 5 (2016) 244–252.
[8] Y.C. Zhou, H.M. Xiang, X.P. Lu, Z.H. Feng, Z.P. Li, J. Adv. Ceram. 4 (2015) 83–93.
[9] C.J. Li, Y. Li, G.J. Yang, C.X. Li, J. Therm. Spray Technol. 22 (2013) 1374–1382.
[10] L. Yang, Q.X. Liu, Y.C. Zhou, W.G. Mao, C. Lu, J. Mater. Sci. Technol. 30 (2014) 371–380.
[11] L.M. He, Z.H. Xu, J.P. Li, R.D. Mu, S.M. He, G.H. Huang, J. Mater. Sci. Technol. 25 (2009) 799–802.
[12] J. Feng, Y.X. Zhou, X.R. Ren, P. Song, W. Pan, J. Am. Ceram. Soc. 101 (2018) 2718–2723.
[13] G.R. Li, H. Xie, G.J. Yang, G. Liu, C.X. Li, C.J. Li, J. Am. Ceram. Soc. 100 (2017) 4240–4251.
[14] D.R. Clarke, M. Oechsner, N.P. Padture, MRS Bull. 37 (2012) 891–902.
[15] A. Cipitria, I.O. Golosnoy, T.W. Clyne, Acta Mater. 57 (2009) 980–992.
[16] G.R. Li, B.W. Lv, G.J. Yang, W.X. Zhang, C.X. Li, C.J. Li, J. Therm. Spray Technol. 24 (2015) 1355–1367.
[17] C.J. Li, A. Ohmori, J. Therm. Spray Technol. 11 (2002) 365–374.
[18] P. Ctibor, R.C. Seshadri, J. Henych, V. Nehasil, Z. Pala, J. Kotlan, J. Adv. Ceram. 5 (2016) 126–136.
[19] W.G. Chi, S. Sampath, H. Wang, J. Am. Ceram. Soc. 91 (2008) 2636–2645.
[20] Y. Tan, J.P. Longtin, S. Sampath, H. Wang, J. Am. Ceram. Soc. 92 (2009) 710–716.
[21] Y. Tan, A. Shyam, W.B. Choi, E. Lara-Curzio, S. Sampath, Acta Mater. 58 (2010) 5305–5315.
[22] H. Xie, Y.C. Xie, G.J. Yang, C.X. Li, C.J. Li, J. Therm. Spray Technol. 22 (2013) 1328–1336.
[23] J.A. Thompson, T.W. Clyne, Acta Mater. 49 (2001) 1565–1575.
[24] N.P. Padture, M. Gell, E.H. Jordan, Science 296 (2002) 280–284.
[25] M. Keshavarz, M.H. Idris, N. Ahmad, J. Adv. Ceram. 2 (2013) 333–340.
[26] G.R. Li, H. Xie, G.J. Yang, G. Liu, C.X. Li, C.J. Li, J. Am. Ceram. Soc. 100 (2017) 2176–2189.
[27] M. Shinozaki, T.W. Clyne, Acta Mater. 61 (2013) 579–588.
[28] G.R. Li, B. Cheng, G.J. Yang, C.X. Li, J. Eur. Ceram. Soc. 37 (2017) 3609–3621.
[29] B. Cheng, N. Yang, Q. Zhang, M. Zhang, Y.M. Zhang, L. Chen, G.J. Yang, C.X. Li, C.J. Li, Ceram. Int. 43 (2017) 15459–15465.
[30] J. Feng, S. Shian, B. Xiao, D.R. Clarke, Phys. Rev. B 90 (2014) 094102.
[31] M. Gell, Mater. Sci. Eng. A 204 (1995) 246–251.
[32] H. Chen, C.X. Ding, J. Inorg. Mater. 17 (2002) 882–886.
[33] R.S. Lima, B.R. Marple, J. Therm, Spray Technol. 16 (2007) 40–63.
[34] M. Gell, E.H. Jordan, Y.H. Sohn, D. Goberman, L. Shaw, T.D. Xiao, Surf. Coat. Technol. 146 (2001) 48–54.
[35] G.R. Li, G.J. Yang, C.X. Li, C.J. Li, J. Eur. Ceram. Soc. 38 (2018) 3325–3332.
[36] D. Chen, F. Luo, X.F. Lou, Y.C. Qing, W.C. Zhou, D.M. Zhu, Ceram. Int. 43 (2017) 4324–4329.
[37] R.S. Lima, B.R. Marple, Mater. Sci. Eng. A 485 (2008) 182–193.
[38] J. Wu, H.B. Guo, L. Zhou, L. Wang, S.K. Gong, J. Therm. Spray Technol. 19 (2010) 1186–1194.
[39] C.G. Zhou, N. Wang, H.B. Xu, Mater. Sci. Eng. A 452 (2007) 569–574.
[40] F.F. Zhou, Y. Wang, L. Wang, Z.Y. Cui, Z.G. Zhang, J. Alloys Compd. 704 (2017) 614–623.
[41] F.F. Zhou, Y. Wang, Z.Y. Cui, L. Wang, J.F. Gou, Q.W. Zhang, C.H. Wang, Ceram. Int. 43 (2017) 4102–4111.
[42] R.S. Lima, A. Kucuk, C.C. Berndt, Mater. Sci. Eng. A 313 (2001) 75–82.
[43] R.S. Lima, A. Kucuk, C.C. Berndt, Mater. Sci. Eng. A 327 (2002) 224–232.
[44] Z. Wang, A. Kulkarni, S. Deshpande, T. Nakamura, H. Herman, Acta Mater. 51 (2003) 5319–5334.
[45] G.R. Li, G.J. Yang, C.X. Li, C.J. Li, Ceram. Int. 43 (2017) 9600–9615.

[46] G.J. Yang, Z.L. Chen, C.X. Li, C.J. Li, J. Therm. Spray Technol. 22 (2013) 1294–1302.
[47] J. Ilavsky, J.K. Stalick, Surf. Coat. Technol. 127 (2000) 120–129.
[48] G.R. Li, G.J. Yang, C.X. Li, C.J. Li, Ceram. Int. 43 (2017) 2252–2266.
[49] G.R. Li, G.J. Yang, C.X. Li, C.J. Li, Ceram. Int. 44 (2018) 2982–2990.
[50] G.R. Li, J. Lei, G.J. Yang, C.X. Li, C.J. Li, J. Eur. Ceram. Soc. 38 (2018) 2579–2587.
[51] G.R. Li, G.J. Yang, C.X. Li, C.J. Li, J. Eur. Ceram. Soc. 37 (2017) 2877–2888.
[52] S. Paul, A. Cipitria, S.A. Tsipas, T.W. Clyne, Surf. Coat. Technol. 203 (2009) 1069–1074.
[53] R. Vassen, N. Czech, W. Mallener, W. Stamm, D. Stover, Surf. Coat. Technol. 141 (2001) 135–140.
[54] N. Wang, C.N. Zhou, S.K. Gong, H.B. Xu, Ceram. Int. 33 (2007) 1075–1081.
[55] J.F. Li, C.X. Ding, J. Mater. Sci. Lett. 18 (1999) 1719–1721.